A Dual-Frequency Resonant Single-Ended IPT Circuit with Enhanced Power Transfer Capability

Jingyu Wang, Zhicong Huang, *Senior Member, IEEE*, and Xiaolu Lucia Li, *Member, IEEE*

***Abstract*—In the design of single-ended inductive power transfer (IPT) converters, the prevalent reliance on the fundamental harmonic approximation (FHA) often results in an underutilization of the input voltage. This paper provides new insights into this problem by deriving and demonstrating that the power transfer capability of a single-ended IPT converter can be enhanced by utilizing the second harmonic component. A novel dual-frequency resonant single-ended IPT converter is designed to allow load-independent voltage output at both the fundamental and second harmonics. This design could improve the power transfer capability without increasing the voltage stress on the power switch. Compared with the conventional single-ended converter with the same output power, the coil currents in the proposed converter are lower. Additionally, the advantages mentioned above are unaffected by coil misalignment. An experimental prototype has been constructed to validate the effectiveness of the proposed method.**

***Index Terms*—Second harmonic, single-ended converter, power transfer capability, inductive power transfer, load-independent output.**

I. INTRODUCTION

INDUCTIVE power transfer (IPT) has revolutionized the way we deliver power, offering a contactless, safe, and convenient solution [1]–[3]. Its applications span a wide range of power levels, from small-scale consumer electronics [4], [5] to biomedical implants [6], and even electric vehicles [7]–[10]. Traditionally, research in IPT has focused on full-bridge (FB) or half-bridge (HB) inverters, mainly due to their flexible control and low voltage stress. These inverters are well-suited for high-power applications [11]–[13]. However, bridgeless converters are gaining popularity in low-power scenarios due to their simplicity and reduced number of switches. They not only simplify the drive circuits but also eliminate the shoot-through risk, making them an ideal choice for low-power IPT systems [14]–[16]. In bridgeless converters, the single-ended type owns higher output power capability and has been widely applied in induction heating [17] and wireless charging [18]. Therefore, single-ended converters are promising in IPT applications.

Extensive research has been dedicated to advancing single-ended IPT converters, particularly in the area of compensation design to achieve constant current (CC) or constant voltage (CV) output and simplify the control strategy. By employing the fundamental harmonic approximation (FHA) analysis approach, it becomes feasible to achieve a load-independent transfer gain for the fundamental harmonic via compensation design. Since high-order harmonics lack resonant channels, their impacts on the output can be disregarded. These principles are applied to customize a single-ended IPT converter to deliver a CC output, a CV output, and even an inherent CC-CV output [19], [20]. However, reactive power in compensation design is often overlooked, leading to increased current in coils. To enhance the output power of single-ended IPT systems, integrated decoupled couplers are incorporated for the parallel connection of two single-ended converters [20], [21]. Expanding on this design approach, a novel inverter topology with independent dual-coil driving capability is proposed with the aim of reducing switch voltage stress when improving output power [22], [23]. However, this method fails to avoid the shoot-through risk of the switches. Additionally, auxiliary LC resonant networks are introduced to enable the parallel connection of three or more single-ended converters, offering higher flexibility to power improvement [24]. Despite these methods for improving output power, their primary focus is on improving the power transfer channel of the fundamental harmonic, with high-order harmonics often being disregarded. Moreover, these methods do not inherently improve the power transfer capability or performance of a single converter. Specifically, the output power in the aforementioned studies depends on the number of single-ended converters for parallel connection.

Based on prior research concerning single-ended IPT converters, a notable challenge in these converters is their heavy dependence on the FHA. It leads to an underestimation or neglect of high-order harmonics, especially the second harmonic, in the converters mentioned. As a result, the full utilization of the input voltage is not achieved, and the potential benefits of utilizing high-order harmonics in single-ended IPT converters have never been explored. To address the problem, this paper first highlights the significance of utilizing the second harmonic in the input voltage of a single-ended IPT converter. Subsequently, a novel dual-frequency single-ended IPT converter is developed to simultaneously utilize the fundamental and second harmonics. The analysis demon-

This work is supported by the Science and Technology Planning Project of Guangdong Province under Grants 2023A0505050124 and 2023B0909050007, the Natural Science Foundation of Guangdong Province under Grant 2023A1515011623, and the Guangzhou Municipal Science and Technology Bureau under Grant 2025A04J7064. (Corresponding author: Zhicong Huang and Xiaolu Lucia Li)

Jingyu Wang and Zhicong Huang are with the Shien-Ming Wu School of Intelligent Engineering, South China University of Technology, Guangzhou, 510006, China (e-mail: zhiconghuang@scut.edu.cn).

Xiaolu Lucia Li is with the School of Integrated Circuits, Sun Yat-sen University, China (email: lixlu8@mail.sysu.edu.cn).

strates that the proposed converter can improve the power transfer capability without increasing the switch voltage stress. Additionally, compared to the conventional single-frequency converter, the proposed design can reduce both the primary coil current and the secondary coil current while maintaining the same level of power transfer. This reduction in current leads to lower power losses and higher power efficiency. The key contributions of this paper are highlighted as follows:

1) The significance of considering and utilizing the second harmonic in the input voltage of a single-ended IPT converter has been unveiled.
2) A novel single-ended IPT converter is proposed to enhance the power transfer capability and achieve a constant voltage (CV) output by creating supplementary resonance and power transfer pathways for the second harmonic.
3) Compared with the conventional single-ended IPT converter, the proposed design has lower primary and secondary coil currents and higher power transfer efficiency.
4) The advantages mentioned above are unaffected by coil misalignment.

The subsequent sections of this paper are structured as follows. In Section II, this paper explores the operating principles of the proposed converter, highlighting the importance of considering the second harmonic component of the input voltage. A general approach is adopted to analyze the feasibility of utilizing the second harmonic to improve the power transfer capability. Section III focuses on the schematic of the proposed converter and the corresponding parameter design. A detailed comparative study between the single-frequency and dual-frequency single-ended IPT converters is presented in Section IV. In Section V, experimental results are provided to validate the effectiveness of the proposed converter. Finally, Section VI concludes the paper.

II. Operating Principles

A. Second-Harmonic Issue

A typical circuit diagram of a single-ended IPT converter is depicted in Fig. 1. It includes only one power switch. The primary coil with the self-inductance L_P is excited by the single-ended driver, which consists of a DC voltage source U_{DC}, a MOSFET switch Q and a resonant capacitor C_P. The secondary coil with the self-inductance L_S is coupled with the primary coil, forming a loosely coupled transformer (LCT) with the mutual inductance M. The LCT is compensated on the secondary side to reduce the voltage-ampere rating and increase the power transfer capability. The high-frequency AC power is rectified to DC power for the load resistance R.

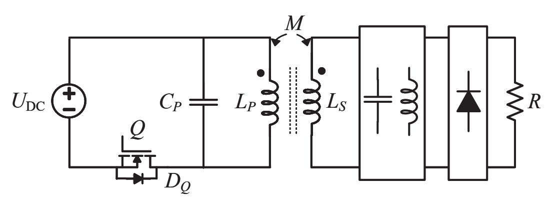

Fig. 1. General circuit diagram of a single-ended IPT converter.

The typical operating waveform of the single-ended IPT driver within a cycle is shown in Fig. 2(a), where u_{C_P} is the voltage across the resonant capacitor C_P. When Q conducts forward or reverse, u_{C_P} is clamped by the DC voltage source U_{DC}. When Q is blocked, the circuit has a source-free response, and u_{C_P} is underdamped. Thus, the operating waveforms can be divided into two modes, i.e., *DC clamped mode* and *underdamped mode*. To analyze the harmonic components of u_{C_P}, a two-step simplification of the operating waveforms is carried out as follows.

1) The waveform of u_{C_P} in the underdamped mode can be approximated as a portion of a sinusoid, as shown in Fig. 2(a). Such that, u_{C_P} can be expressed as a piecewise function given by

$$u_{C_P}(t) = \begin{cases} -A\sin(\omega_0 t + \varphi), & 0 \le t < t_1 \\ U_{\mathrm{DC}}, & t_1 \le t \le T \end{cases}, \tag{1}$$

where A, ω_0, and φ are the amplitude, frequency, and phase angle of the sinusoid, respectively. Since u_{C_P} is a periodic waveform, $u_{C_P}(0) = U_{\mathrm{DC}}$ can be derived.

2) The waveform of u_{C_P} in the short intervals (0, t_a) and (t_b, t_1) can be linearized, such that sections ① and ② can be approximated as triangles. The duration of these two intervals is identical donated as Δt and can be calculated by

$$\Delta t = t_a - 0 = t_1 - t_b = \frac{\pi \arcsin(\frac{U_{\mathrm{DC}}}{A})}{180\mathrm{deg}\omega_0}. \tag{2}$$

As shown in Fig. 2(b), sections ① and ② can be merged as a rectangular section ①+②. Thus, u_{C_P} can be reshaped as a new waveform to simplify the calculation, i.e.,

$$u_{C_P}(t) = \begin{cases} 0, & 0 \le t < t_a \\ -A\sin[\omega_0(t - t_a)], & t_a \le t < t_b \\ U_{\mathrm{DC}}, & t_b \le t \le T \end{cases}. \tag{3}$$

To obtain the amplitude of arbitrary harmonics of $u_{C_P}(t)$, ω_0 and A should be calculated first.

According to the above analysis, ω_0 could be expressed by

$$\omega_0 = \frac{\pi}{t_b - t_a} = \frac{\pi}{(1 - D - D_{\mathrm{Z}})T - 2\Delta t}, \tag{4}$$

where D is the duty cycle of the switch Q and D_{Z} is the zero-voltage-switching (ZVS) margin of the switch.

When calculating A, the principle of voltage-second balance on C_P within a cycle should be applied:

$$U_{\mathrm{DC}}(T - t_b) = \int_{t_a}^{t_b} A\sin[\omega_0(t - t_a)]\mathrm{d}t = \frac{2A}{\pi}(t_b - t_a). \tag{5}$$

With (3), (4) and (5), A can be derived as

$$A = \frac{\pi U_{\mathrm{DC}} \cdot [(D + D_{\mathrm{Z}})T + \Delta t]}{2\left[(1 - D - D_{\mathrm{Z}})T - 2\Delta t\right]}. \tag{6}$$

After obtaining both ω_0 and A, the curve in Fig. 2(b) can be decomposed into its Fourier components, as given by (7).

$$u_{C_P}(t) = \sum_{n=1}^{\infty} \left[a_n \cos(n\omega_{\mathrm{s},1} t) + b_n \sin(n\omega_{\mathrm{s},1} t)\right], \tag{7}$$

$$a_n = \frac{2}{T}\int_{t_a}^{t_b} (-A)\sin(\omega_0 t)\sin(n\omega_{s,1}t)dt + \frac{2}{T}\int_{t_b}^{T} U_{DC}\sin(n\omega_{s,1}t)dt, \tag{8a}$$

$$b_n = \frac{2}{T}\int_{t_a}^{t_b} (-A)\sin(\omega_0 t)\cos(n\omega_{s,1}t)dt + \frac{2}{T}\int_{t_b}^{T} U_{DC}\cos(n\omega_{s,1}t)dt. \tag{8b}$$

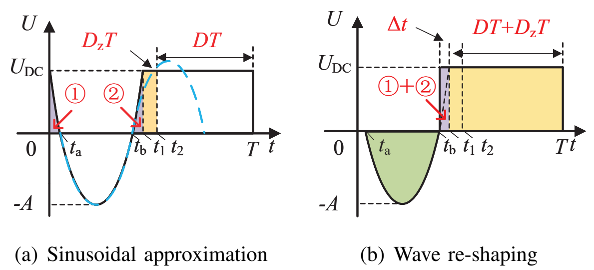

Fig. 2. Simplification of the waveform of u_{C_P} for calculation.

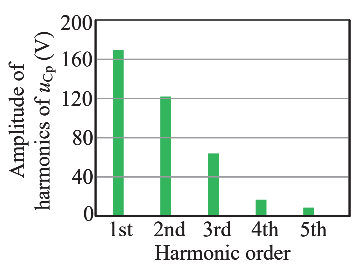

Fig. 3. Calculated harmonic components of u_{C_P}.

where a_n and b_n are calculated by equations (8a) and (8b) respectively, $\omega_{s,1}$ is the operating frequency, and $n\omega_{s,1} = \omega_{s,n}$.

Therefore, the amplitude of arbitrary harmonics of u_{C_P} can be expressed as

$$U_{C_P,n} = \sqrt{a_n^2 + b_n^2}. \tag{9}$$

For example, a single-ended IPT converter with circuit parameters given in Table I is considered. Based on (9), the harmonic components of u_{C_P} can be calculated and plotted in Fig. 3. To discern the parameters associated with these harmonics, the subscript "1" will represent the fundamental component, while the subscript "2" signifies the second-order harmonic. By referring to Fig. 3, the second harmonic holds notable importance and a relationship between the fundamental and second components of u_{C_P} as $U_{C_P,2} \approx 0.68U_{C_P,1}$ can be established for the subsequent analysis and design.

TABLE I
PARAMETER DESIGN OF THE SINGLE-ENDED IPT DRIVER

Parameter	Definition	Value
f_s	Operating frequency	100 kHz
U_{DC}	Output DC voltage	96 V
D	Duty cycle	0.5
D_Z	ZVS margin	0.08

B. Enhancement of Power Transfer Capability by Utilizing Second Harmonic

According to the above analysis, the single-ended IPT converter could be expressed by Fig. 4 and simplified by Thevenin's Theorem and Norton's Theorem. In this representation, the single-ended IPT driver is symbolized as a voltage source with harmonics, while the LCT is portrayed as a T circuit. Additionally, $i_P(t)$ and $i_S(t)$ denote the primary coil current and the secondary coil current, respectively, while $u_o(t)$ represents the output AC voltage.

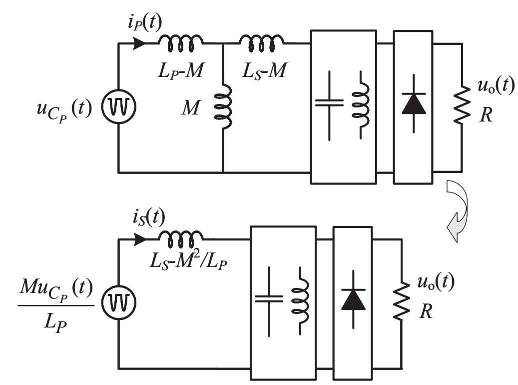

Fig. 4. Simplified process of the single-ended IPT converter.

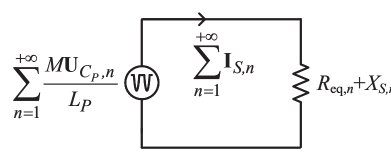

Fig. 5. Multi-frequency resonant circuit model.

In general, the power transfer capability of the single-ended IPT converter is given by

$$P_{out} = \sum_{n=1}^{\infty} S_n Q_n, \tag{12}$$

where S_n and Q_n are the uncompensated apparent power and the tuned load quality factor at the nth harmonic, respectively. The value of S_n represents the multiplication of the open-circuit voltage ($U_{oc,n}$) and the short-circuit current ($I_{sc,n}$) of the secondary coil. This can be expressed as $S_n = U_{oc,n}I_{sc,n}$. The relevant parameters can be calculated according to Fig. 4. On the other hand, the value of Q_n is determined by the specific load condition [25].

Based on the simplified circuit in Fig. 4, the circuit shown in Fig. 5 can be further obtained when the compensation network and rectifier bridge are converted.

For a conventional single-ended IPT converter, only the fundamental harmonic is resonant and subject to the following relationship.

$$\begin{cases} R_{\mathrm{eq},n} = R_{\mathrm{eq,con}} & n = 1 \\ X_{S,n} = 0 & n = 1 \\ R_{\mathrm{eq},n} \approx 0 & n > 1 \\ X_{S,n} = \infty & n > 1 \end{cases}, \tag{13}$$

where $R_{\mathrm{eq,con}}$ is constant and proportional to the load R. The power transfer capability of a conventional single-ended converter can be derived as

$$P_{\mathrm{out},1} = S_1 Q_1 = \frac{U_{C_P,1}^2 M^2 Q_1}{2\omega_{\mathrm{s},1} L_P^2 \left(L_S - M^2/L_P\right)} \tag{14}$$

where Q_1 could be calculated by (15), and $Q_n(n > 1) \approx 0$ due to (13).

$$Q_1 = \frac{L_S - M^2/L_P}{R_{\mathrm{eq,con}}}. \tag{15}$$

The output power can usually be adjusted by changing the value of $U_{C_P,1}$ and Q_1. Although it is straightforward to improve the power transfer capability by increasing the input DC voltage U_{DC} to apply a high $U_{C_P,1}$, it suffers from the voltage tolerance of the switching device. Moreover, excessively high Q_1 may lead to a reduction in circuit bandwidth. Therefore, a new approach regardless of $U_{C_P,1}$ and Q_1 should be developed to improve the power transfer capability.

If a single-ended IPT converter is resonant at both the fundamental and second harmonics, the following relationship is established.

$$\begin{cases} R_{\mathrm{eq},n} = R_{\mathrm{eq,pro1}} & n = 1 \\ X_{S,n} = 0 & n = 1 \\ R_{\mathrm{eq},n} = R_{\mathrm{eq,pro2}} & n = 2 \\ X_{S,n} = 0 & n = 2 \\ R_{\mathrm{eq},n} \approx 0 & n > 2 \\ X_{S,n} = \infty & n > 2 \end{cases}, \tag{16}$$

where both $R_{\mathrm{eq,pro1}}$ and $R_{\mathrm{eq,pro2}}$ are constant and proportional to the load R.

When $R_{\mathrm{eq,pro1}} = R_{\mathrm{eq,con}}$, the power transfer capability of the dual-frequency single-ended converter is a superposition given by

$$\begin{aligned} P_{\mathrm{out},1+2} &= P_{\mathrm{out},1} + P_{\mathrm{out},2} \\ &= \frac{U_{C_P,1}^2 M^2 Q_1}{2\omega_{\mathrm{s},1} L_P^2 \left(L_S - \frac{M^2}{L_P}\right)} + \frac{U_{C_P,2}^2 M^2 Q_2}{2\omega_{\mathrm{s},2} L_P^2 \left(L_S - \frac{M^2}{L_P}\right)} \end{aligned} \tag{17}$$

where Q_2 could be calculated by (18), and $Q_n(n > 2) \approx 0$ due to (16).

$$Q_2 = \frac{L_S - M^2/L_P}{R_{\mathrm{eq,pro2}}}. \tag{18}$$

From (14) and (17), it can be readily derived

$$P_{\mathrm{out},1+2} > P_{\mathrm{out},1}. \tag{19}$$

This indicates that the compensation design enabling second harmonic utilization can help enhance the power transfer capability for a single-ended IPT converter.

III. Circuit Structure and Parameter Design

A. Schematic of Proposed Converter

To enable power transfer at both the fundamental and second harmonics, a dual-frequency compensation network comprising two resonant tanks needs to be designed. Additionally, achieving a load-independent voltage output should also be considered to simplify the output control.

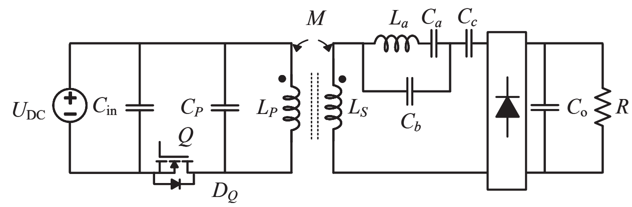

Fig. 6. Proposed dual-frequency resonant single-ended IPT converter.

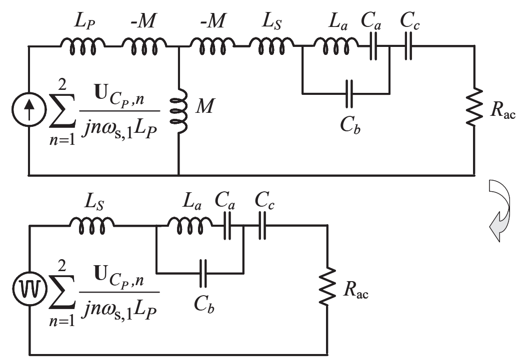

Fig. 7. Equivalent circuit of the proposed dual-frequency resonant single-ended IPT converter.

Based on the abovementioned considerations, the proposed single-ended IPT converter with dual-frequency compensation is illustrated in Fig. 6. The primary side of the converter remains unchanged from the conventional single-ended IPT converter [21], comprising a single-ended IPT driver and a primary coil. On the secondary side, the compensation circuit consists of three capacitors (C_a, C_b, and C_c) and an inductor (L_a). Specifically, C_a and L_a are connected in series, while C_b is connected in parallel with them.

To obtain the equivalent circuit, the harmonics of the current in L_P could be expressed by

$$I_{P,n} = |\mathbf{I}_{P,n}| = \frac{U_{C_P,n}}{|jn\omega_{\mathrm{s},1} L_P + R_{S,n}|} \approx \frac{U_{C_P,n}}{n\omega_{\mathrm{s}} L_P} (n = 1 \ or \ 2), \tag{20}$$

where

$$R_{S,n} = \frac{\omega_{\mathrm{s},n}^2 M^2}{R_{\mathrm{eq},n}}. \tag{21}$$

The equivalent circuit of the proposed design can then be derived, as shown in Fig. 7, where R_{ac} is the AC resistance of the secondary circuit and can be expressed by

$$R_{\mathrm{ac}} = \frac{8R}{\pi^2}. \tag{22}$$

Equation (22) is valid at any harmonic orders, which has been discussed in the previous research [26].

B. Parameter Design of Compensation Circuit

The derivation process using Thevenin's Theorem and Norton's Theorem is shown in Figs. 8 and 9. Here, $\mathbf{U}_{C_P,1}$, $\mathbf{U}_{C_P,2}$, $\mathbf{U}_{o,1}$, $\mathbf{U}_{o,2}$, $\mathbf{I}_{P,1}$, $\mathbf{I}_{P,2}$, $\mathbf{I}_{S,1}$and $\mathbf{I}_{S,2}$ are vectors of fundamental and second harmonics of $u_{C_P}(t)$, $u_o(t)$, $i_P(t)$ and $i_S(t)$, respectively. When considering the fundamental harmonic, the derivation process is shown in Fig. 8. The compensation design aims to form a resonant tank at the fundamental harmonic and achieve a load-independent voltage output. To realize this, the C_a-L_a network in the purple box is resonant, and the remaining C_c resonates with L_S. The compensation design should satisfy

$$\begin{cases} -j\omega_{\mathrm{s},1}L_a = \dfrac{1}{j\omega_{\mathrm{s},1}C_a} \\ \dfrac{1}{j\omega_{\mathrm{s},1}C_c} = -j\omega_{\mathrm{s},1}L_S \end{cases}. \tag{23}$$

From Fig. 8, when (23) is satisfied, the output voltage is identical to the input voltage, i.e.,

$$U_{\mathrm{o},1} = |\mathbf{U}_{\mathrm{o},1}| = \frac{MU_{C_P,1}}{L_P}. \tag{24}$$

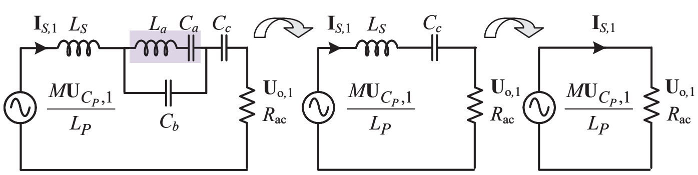

Fig. 8. Derivation process using Thevenin's Theorem and Norton's Theorem at the fundamental harmonic.

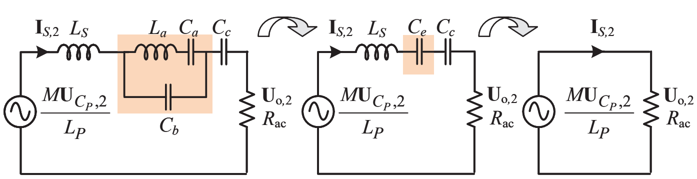

Fig. 9. Derivation process using Thevenin's Theorem and Norton's Theorem at the second harmonic.

For the second harmonic, the derivation process is similar, as depicted in Fig. 9. To form a resonant tank at the second harmonic and provide a load-independent voltage, the C_a-L_a-C_b network in the orange box denotes an equivalent capacitance C_e, and then the C_e-C_c network resonates with L_S. Thus, the compensation design should satisfy

$$\begin{cases} \dfrac{1}{j\omega_{\mathrm{s},2}C_e} = \dfrac{(j\omega_{\mathrm{s},2}L_a + \frac{1}{j\omega_{\mathrm{s},2}C_a})\frac{1}{j\omega_{\mathrm{s},2}C_b}}{j\omega_{\mathrm{s},2}L_a + \frac{1}{j\omega_{\mathrm{s},2}C_a} + \frac{1}{j\omega_{\mathrm{s},2}C_b}} \\ \dfrac{1}{j\omega_{\mathrm{s},2}C_c} + \dfrac{1}{j\omega_{\mathrm{s},2}C_e} + j\omega_{\mathrm{s},2}L_S = 0 \end{cases}. \tag{25}$$

From Fig. 9, the output voltage $U_{\mathrm{o},2}$ at the second harmonic is also identical to the input voltage given by

$$U_{\mathrm{o},2} = |\mathbf{U}_{\mathrm{o},2}| = \frac{MU_{C_P,2}}{L_P}. \tag{26}$$

According to equations (24) and (26), both $U_{\mathrm{o},1}$ and $U_{\mathrm{o},2}$ are load-independent. And $R_{\mathrm{eq,pro1}} = R_{\mathrm{eq,pro2}} = R_{\mathrm{ac}}$ as shown in Figs. 8 and 9. As a result, the load-independent DC output voltage can be expressed by (27).

$$U_{\mathrm{OUT}} = \sqrt{\left(\frac{\pi U_{\mathrm{o},1}}{4}\right)^2 + \left(\frac{\pi U_{\mathrm{o},2}}{4}\right)^2}. \tag{27}$$

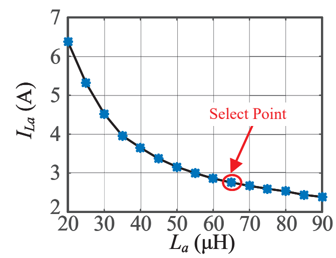

Fig. 10. Relationship between I_{La} and L_a.

Based on the above analysis, it is clear that the compensation components, namely C_a, L_a, and C_b, offer a certain degree of design flexibility. As the primary source of power losses in the converter stems from the inductive devices, optimizing the value of L_a becomes important. Once the parameters for the LCT and the operating frequency are determined, the current in L_a plotted against the inductance of L_a in Fig. 10 could be obtained. As the inductance of L_a increases, the rate at which the decrease of the current I_{La} slows down. Therefore, it is advisable to select a point where the current in L_a starts varying slowly. This choice helps reduce both the cost and power losses of the converter. In this paper, it is recommended to use a value of approximately 65 μH for L_a. Subsequently, C_a and C_b can be calculated using (23) and

$$C_b = \frac{L_S + L_a}{3\omega_{\mathrm{s},1}^2 L_a L_S}. \tag{28}$$

With these calculations, the parameters outlined in this paper can be determined. The design process is shown in Fig. 11, and the parameters are listed in Table II. The design procedure of the proposed circuit can be summarized as follows.

1) Obtain critical system parameters, including U_{DC}, U_{OUT}, D, $D_{\mathrm{Z,ref}}$, $\omega_{\mathrm{s},1}$, L_P and L_S.
2) Calculate AC input voltages $U_{C_P,1}$ and $U_{C_P,2}$, determine the mutual inductance M, and then calculate the compensation parameters in the receiving circuit.
3) Assign an initial value to C_P, conduct circuit simulations, and adjust C_P until $D_{\mathrm{Z}} = D_{\mathrm{Z,ref}}$.

IV. Comparison Between Single-Frequency and Dual-Frequency Converters

A. Voltage Transfer Gain

A typical single-frequency single-ended IPT converter is shown in Fig. 12, where $G(f_{\mathrm{s}}) = u_{\mathrm{o}}(f_{\mathrm{s}})/u_{C_P}(f_{\mathrm{s}})$ is used

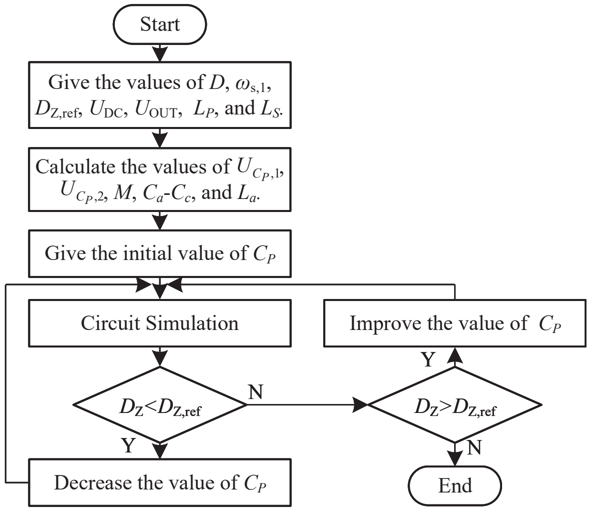

Fig. 11. Design process.

TABLE II
PARAMETER DESIGN OF PROPOSED CONVERTER

Symbol	Definition	Value
C_P	Primary-side compensation capacitor	16.02 nF
L_a	Secondary-side compensation inductor	65.01 μH
C_a	Primary-side compensation capacitor	39.02 nF
C_b	Primary-side compensation capacitor	24.94 nF
C_c	Primary-side compensation capacitor	35.84 nF
L_P	Inductance of the transmitter coil	70.80 μH
L_S	Inductance of the secondary coil	70.67 μH
C_{in}	Input filter capacitor	47 μF
C_{o}	Output filter capacitor	100 μF
M	Mutual inductance	26.29 μH
f_{s}	Operating frequency	100 kHz
$U_{C_P,1}$	Calculated amplitude of fundamental harmonic	165 V
$U_{C_P,2}$	Calculated amplitude of second harmonic	113 V
U_{DC}	Input DC voltage	96 V
$U_{\text{OUT,pro}}$	Output DC voltage	56 V
D	Duty cycle	0.5
D_{ZVS}	ZVS margin	0.08

to represent the output characteristics at different operating frequencies. The transfer gain of the single-frequency single-ended IPT converter with respect to the operating frequency is illustrated in Fig. 13(a), which has only one load-independent point with the operating frequency being 100 kHz. The corresponding parameter design is detailed in Table III.

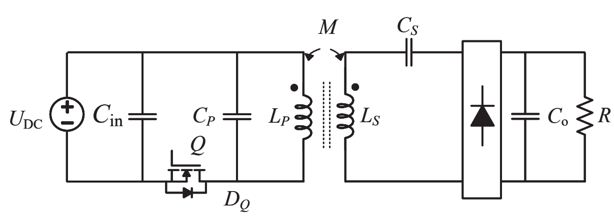

Fig. 12. Conventional single-frequency single-ended IPT converter with P-S compensation [21].

Similarly, Fig. 13(b) displays the voltage transfer gain of the proposed converter. Unlike the relationship depicted in Fig. 13(a), there are two load-independent points with operating frequencies being 100 kHz and 200 kHz. This implies that both the fundamental and second harmonics can be utilized for the resonant power transfer and load-independent output. Notably, both of these resonant points are located at the extreme points.

TABLE III
PARAMETER DESIGN OF COMPARED CONVERTER

Symbol	Definition	Value
C_P	Primary-side compensation capacitor	16.02 nF
C_S	Primary-side compensation capacitor	41.59 nF
L_P	Inductance of the transmitter coil	70.80 μH
L_S	Inductance of the secondary coil	70.67 μH
M	Mutual inductance	26.29 μH
C_{in}	Input filter capacitor	47 μF
C_{o}	Output filter capacitor	100 μF
f_{s}	Operating frequency	100 kHz
$U_{C_P,1}$	Calculated amplitude of fundamental harmonic	165 V
U_{DC}	Input DC voltage	96 V
$U_{\text{OUT,con}}$	Output DC voltage	48 V
D	Duty cycle	0.5
D_{Z}	ZVS margin	0.08

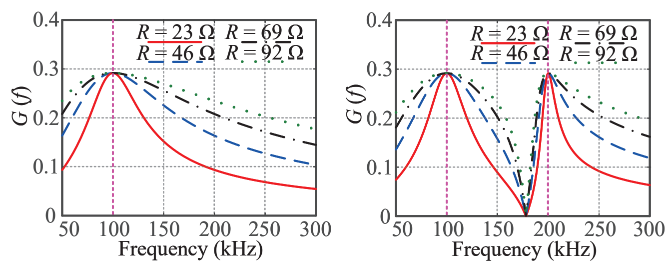

(a) Voltage transfer gain of the conventional converter. (b) Voltage transfer gain of the proposed converter.

Fig. 13. Voltage transfer gains of conventional and proposed converters.

B. Coil Current

When considering the second harmonic for power transfer in a single-ended IPT converter, it is essential to note that this impacts both the primary coil current and the secondary coil current. To highlight the advantages of the dual-frequency converter over the conventional single-frequency converter, a comparison is made between the proposed dual-frequency and single-frequency converters with the same output power. In this comparison, the subscript "con" is used for the single-frequency converter, while the subscript "pro" is used to denote the dual-frequency converter. Suppose the two converters have the same primary circuit and LCT. When the output power of these two converters is the same, the output power could be expressed by

$$
\begin{aligned}
P_{\text{out}} &= i_{S,\text{con}}^2 R_{\text{eq,con}} = \frac{U_{C_P,1}^2 M^2}{2L_P^2 R_{\text{eq,con}}} \\
&= i_{S,\text{pro}}^2 R_{\text{eq,pro}} = \frac{U_{C_P,1}^2 M^2}{2L_P^2 R_{\text{eq,pro1}}} + \frac{U_{C_P,2}^2 M^2}{2L_P^2 R_{\text{eq,pro2}}},
\end{aligned}
\tag{29}
$$

where $i_{S,\text{pro}}$ is the RMS value of secondary coil current of the proposed converter and $i_{S,\text{con}}$ is the RMS value of secondary coil current of the conventional converter, and $R_{\text{eq,pro}} = R_{\text{eq,pro1}} = R_{\text{eq,pro2}} = R_{\text{ac}}$ in this paper. Moreover, $R_{\text{eq,pro}} = (U_{C_P,1}^2 + U_{C_P,2}^2) R_{\text{eq,con}} / U_{C_P,1}^2$ when the two converters have the same output power. Then, the relationship as shown in (30) could be obtained

$$\frac{i_{S,\mathrm{pro}}}{i_{S,\mathrm{con}}}=\sqrt{\frac{U_{C_P,1}^2}{U_{C_P,1}^2+U_{C_P,2}^2}}<1. \tag{30}$$

The primary coil currents can be expressed by (31)-(34).

$$I_{P,\mathrm{con1}}=|\frac{MU_{C_P,1}/L_P+\mathbf{I}_{S,\mathrm{con1}}(-j\omega_{\mathrm{s},1}\frac{M^2}{L_P})}{j\omega_{\mathrm{s},1}M}|, \tag{31}$$

$$I_{P,\mathrm{con2}}=|\frac{MU_{C_P,2}/L_P+\mathbf{I}_{S,\mathrm{con2}}(-j\omega_{\mathrm{s},2}\frac{M^2}{L_P})}{j\omega_{\mathrm{s},2}M}|, \tag{32}$$

$$I_{P,\mathrm{pro1}}=|\frac{U_{C_P,1}}{j\omega_{\mathrm{s},1}M}|, \tag{33}$$

$$I_{P,\mathrm{pro2}}=|\frac{U_{C_P,2}}{j\omega_{\mathrm{s},2}M}|. \tag{34}$$

According to the calculation results, $I_{P,\mathrm{con1}}>I_{P,\mathrm{pro1}}$ and $I_{P,\mathrm{con2}}>I_{P,\mathrm{pro2}}$, therefore

$$\frac{i_{P,\mathrm{pro}}}{i_{P,\mathrm{con}}}=\sqrt{\frac{I_{P,\mathrm{pro1}}^2+I_{P,\mathrm{pro2}}^2}{I_{P,\mathrm{con1}}^2+I_{P,\mathrm{con2}}^2}}<1, \tag{35}$$

where $i_{P,\mathrm{pro}}$ is the RMS value of the primary coil current of the proposed converter and $i_{P,\mathrm{con}}$ is the RMS value of the primary coil current of the conventional converter.

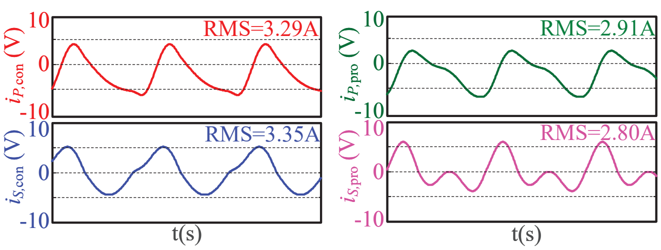

(a) $i_{P,\mathrm{con}}$ and $i_{S,\mathrm{con}}$. (b) $i_{P,\mathrm{pro}}$ and $i_{S,\mathrm{pro}}$.

Fig. 14. Simulation results of the conventional and proposed converters when the output power is 136 W.

It can be found that the proposed dual-frequency single-ended IPT converter has lower primary coil current and secondary coil current than that of the single-frequency converter with the same output power. Using the parameter design in Table II and Table III, the preliminary simulation results are shown in Fig. 14. The results agree with the previous theoretical analysis.

V. Experimental Evaluation

A prototype with the output power being 136 W is built to verify the above analysis, as shown in Fig. 15(a). Two coaxial circular coils with a diameter being 22.8 cm are utilized for both the transmitter and receiver, forming the LCT with a 5 cm gap distance. These coils are constructed using Litz wires with the wire diameter being 3 mm. Each coil consists of 16-turn Litz wires and is covered by ferrite material. More details are shown in Fig. 15(b). The type of the SiC MOSFET is CGE1M120080 and the type of the secondary-side rectifier is MBR20150. An electronic load is employed to simulate the equivalent load.

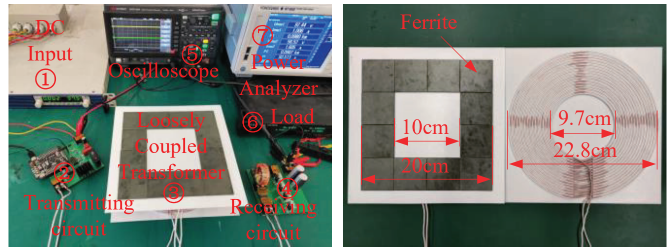

(a) Platform. (b) LCT.

Fig. 15. Photograph of the proposed dual-frequency single-ended IPT converter.

A. Switching and Output Features

Fig. 16(a) shows the soft-switching waveforms when the equivalent load is 23 Ω and Fig. 16(b) shows the soft-switching waveforms when the equivalent load is 46 Ω. When the operating frequency is 100 kHz, and the duty cycle is 50%, the measured amplitude of the drain-source voltage of the switch (i.e., $U_{\mathrm{DS}}(t)$) is 425 V at 23 Ω and 429 V at 46 Ω. The ZVS margin is almost unaffected when the load changes. In Fig. 17, waveforms of $U_{\mathrm{OUT,pro}}$ and $I_{\mathrm{OUT,pro}}$ of the proposed converter when the equivalent load changes are presented. The experimental results show that the output voltage is approximately 56 V, which proves that the output voltage of the proposed converter is load-independent.

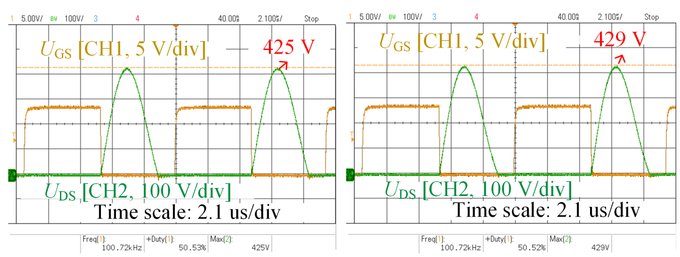

(a) Waveforms of ZVS when the load is 23 Ω. (b) Waveforms of ZVS when the load is 46 Ω.

Fig. 16. Waveforms of ZVS.

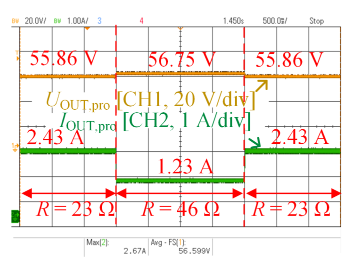

Fig. 17. Output waveforms when the load R changes.

B. Power Transfer Capability

To prove that the proposed dual-frequency single-ended IPT converter has enhanced power transfer capability, a comparison with the single-frequency converter should be conducted. "S-F" denotes the single-frequency converter. As discussed in Section II-B, $R_{\mathrm{eq,pro1}} = R_{\mathrm{eq,con}} = 8R/\pi^2$ should be satisfied, which means that the two converters have the same Q_1. Taking the single-frequency converter shown in Fig. 12 as an example, the single-frequency and dual-frequency converters have the same primary circuit and LCT as designed in Table III, and the load-independent output voltage $U_{\mathrm{OUT,con}}$ is 48 V.

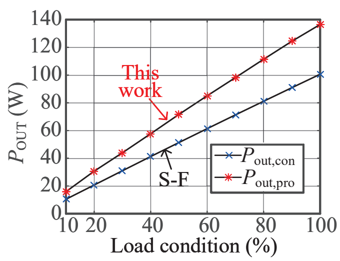

Fig. 18. Output power versus the load of the proposed (pro) dual-frequency and the conventional (con) single-frequency single-ended IPT converters.

When R changes from 230 Ω to 23 Ω, the measured output-power trends of the two converters are shown in Fig. 18. Obviously, the proposed dual-frequency single-ended IPT converter has higher power transfer capability when the two converters have the same Q_1.

C. Coil Current

When the output power of both the single-frequency and dual-frequency single-ended IPT converters is 136 W, the coil current waveforms are shown in Fig. 19. The proposed converter has a load-independent output voltage of 56 V, and the load is 23 Ω. Still taking the single-frequency converter shown in Fig. 12 as an example, its parameter design is shown in Table III, which has a load-independent output voltage of 48 V, and the load is 16.9 Ω. For the single-frequency converter, $i_{P,\mathrm{con}}$ is 3.355 A and $i_{S,\mathrm{con}}$ is 3.476 A, while $i_{P,\mathrm{pro}}$ is 3.085 A and $i_{S,\mathrm{pro}}$ is 2.933 A for the proposed converter. It is obvious that $i_{P,\mathrm{pro}} < i_{P,\mathrm{con}}$ and $i_{S,\mathrm{pro}} < i_{S,\mathrm{con}}$. Fig. 20 provides the Fourier analysis of the coil currents of the two converters.

D. Efficiency

Fig. 21(a) shows the efficiency performance of the single-frequency converter and the proposed dual-frequency converter. Particularly, η_{con} is the efficiency of the converter in Fig. 12, and η_{pro} is the efficiency of the proposed converter. We can find that the proposed converter is superior in efficiency, with the maximum efficiency being about 92.9%. The power loss distribution is shown in Fig. 21(b), where "S-F" denotes the single-frequency converter. The proposed method significantly reduces power losses attributed to the LCT by decreasing both the primary coil current and the secondary coil current. Moreover, by decreasing the current in the receiving coil, power losses in the rectifier are reduced as well. Despite the introduction of more passive components, the increase in power losses is outweighed by the reduction in power losses. As a result, the proposed method achieves an overall efficiency improvement.

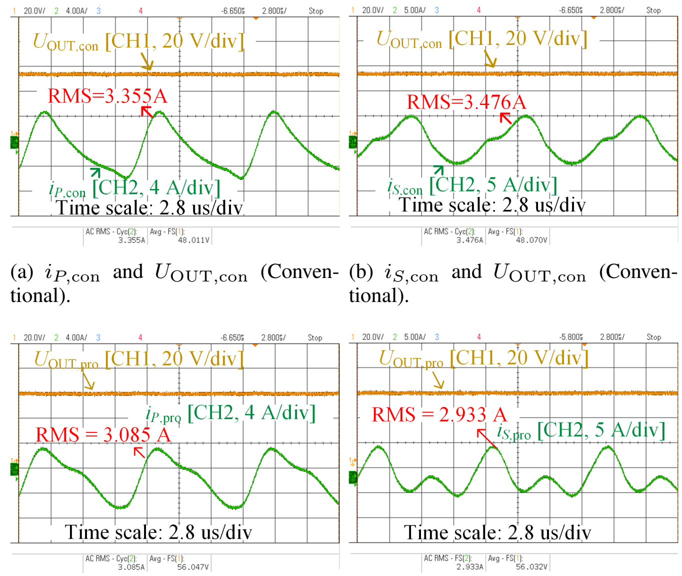

(a) $i_{P,\mathrm{con}}$ and $U_{\mathrm{OUT,con}}$ (Conventional). (b) $i_{S,\mathrm{con}}$ and $U_{\mathrm{OUT,con}}$ (Conventional). (c) $i_{P,\mathrm{pro}}$ and $U_{\mathrm{OUT,pro}}$ (Proposed). (d) $i_{S,\mathrm{pro}}$ and $U_{\mathrm{OUT,pro}}$ (Proposed).

Fig. 19. Coil current waveforms of the conventional and proposed converters when the output power is 136 W.

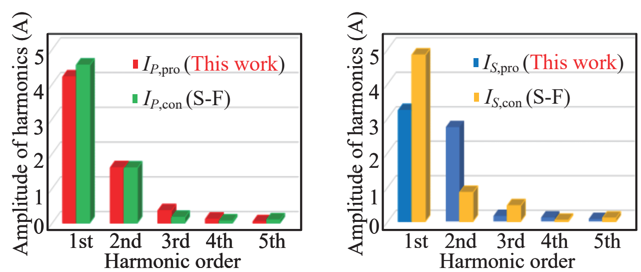

(a) Primary coil. (b) Secondary coil.

Fig. 20. Fourier analysis of the coil currents of the proposed (pro) dual-frequency and conventional (con) single-frequency converters.

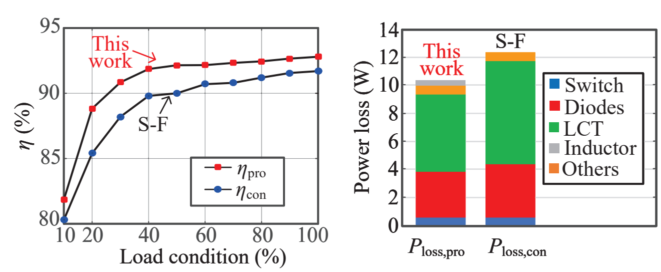

(a) Efficiency. (b) Power losses.

Fig. 21. Efficiency versus the load of the proposed (pro) dual-frequency and the conventional (con) single-frequency single-ended IPT converters when the output power is 136 W.

TABLE IV
COMPARISON WITH EXISTING WORK

Reference	Topology	Number of switches	Drive circuit design	Shoot-through problem	Harmonic order used for power transfer	Power transfer capability improvement	Protection against removal of receiver
Proposed	Single-switch	1	Simple	No	Fundamental+Second	Yes	Yes
[20]	Single-switch	1	Simple	No	Fundamental	No	Yes
[7]	Full-bridge	4	Complex	Yes	Fundamental	No	No
[8]	Full-bridge	4	Complex	Yes	Fundamental	No	Yes
[27]	Class-E	1	Simple	No	Fundamental	No	No
[22]	Dual-switch	2	Medium	Yes	Fundamental	No	No
[23]	Dual-switch	2	Medium	Yes	Fundamental	No	No

E. Performance with Coil Misalignment

Given the symmetrical coil design in this study, our analysis focuses solely on misalignment along the x-direction. Fig. 22(b) compares the efficiency of the proposed and conventional single-ended IPT converters with respect to coil misalignment. To ensure a fair comparison, conditions such as the accuracy of compensation parameters, heat dissipation, and ZVS conditions were controlled to be as consistent as possible for both converters. It can be observed that increased coil misalignment results in a notable drop in the efficiency of the conventional one. This is because the typical compensation network of a conventional single-ended converter is designed to compensate for the inductance $L_S - M^2/L_P$ in the receiving coil [21]. As misalignment increases, mutual inductance M decreases, which leads to detuning and a great reduction in the efficiency of the conventional converter. This issue is not sharp in our design, since the corresponding compensation network is used to compensate for the inductance L_S of the receiving coil instead of $L_S - M^2/L_P$. Furthermore, both the primary coil current and secondary coil current of the conventional converter are higher than that of the proposed converter. These factors contribute to a more significant change in efficiency for the conventional converter compared to the proposed converter.

Table IV conducts a comparison of the proposed converter with other typical IPT converters. Although the proposed method may not provide the same level of flexible primary-side control as a full-bridge converter, it uses only one switch. This feature significantly simplifies the drive circuit, lowers the cost, and notably eliminates the shoot-through problem, thereby improving the overall reliability.

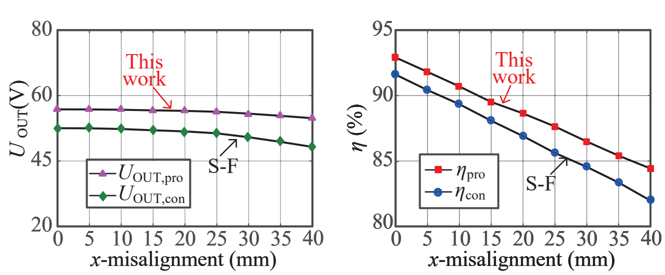

(a) Output voltage. (b) Efficiency.

Fig. 22. Circuit performance when coil misalignment occurs.

VI. CONCLUSION

In this paper, the significance of the second harmonic in single-ended IPT converters has been demonstrated, showing its potential to enhance the power transfer capability. On this basis, we develop a novel single-ended IPT converter, featuring a dual-frequency compensation network. This design utilizes both the fundamental and second harmonics for wireless power transfer, reducing both the primary coil current and secondary coil current while achieving a load-independent output voltage. The corresponding analysis highlights how this dual-frequency approach improves the power transfer capability. Despite the complexity of simultaneously addressing dual-frequency resonance and load independence through the compensation network, a detailed design methodology is presented, offering a systematic pathway for practical applications. An experimental prototype with an output power of 136 W is constructed for validation. Experimental results demonstrate that the proposed design outperforms conventional single-ended IPT converters in power transfer capability. And the effective utilization of the second harmonic could improve operating efficiency by reducing coil currents. Given that these advantages can be maintained even under conditions of coil misalignment, we can also use the design methodology in misaligned scenarios.

High-order harmonics will be explored in the future to provide supplementary power support in the presence of coil misalignment. This approach will contribute to ensuring stable power transfer in IPT systems when confronted with the challenge of misalignment.

REFERENCES

[1] X. Dai, X. Li, Y. Li, and A. P. Hu, "Maximum efficiency tracking for wireless power transfer systems with dynamic coupling coefficient estimation," *IEEE Trans. Power Electron.,* vol. 33, no. 6, pp. 5005–5015, Jun. 2018.

[2] Y. Sun, H. Zhang, A. P. Hu, C. S. Tang, and L. J. Xiang, "The recognition and control of nonideal soft-switching frequency for wireless power transfer system based on waveform identification," *IEEE Trans. Power Electron.,* vol. 32, no. 8, pp. 6617–6627, Aug. 2017.

[3] Y. Gong, Z. Zhang, and S. Chang, "Single-transmitter-controlled multiple-channel constant current outputs for in-flight wireless charging of drones," *IEEE Trans. Ind. Electron.,* vol. 71, no. 4, pp. 3606–3616, Apr. 2024.

[4] J. Lee, B. Bae, B. Kim, J. Lim, and B. Lee, "A load-independent battery charging system for multiple wearable devices using conductive textile," *IEEE Trans. Ind. Electron.,* vol. 71, no. 11, pp. 15211–15215, Nov. 2024.

[5] J. Zhou, B. Zhang, W. Xiao, D. Qiu, and Y. Chen, "Nonlinear parity-time-symmetric model for constant efficiency wireless power transfer: application to a drone-in-flight wireless charging platform," *IEEE Trans. Ind. Electron.,* vol. 66, no. 5, pp. 4097–4107, May 2019.

[6] R. Sedehi, D. Budgett, J. Jiang, and X. Ziyi, "A wireless power method for deeply implanted biomedical devices via capacitively coupled conductive power transfer," *IEEE Trans. Power Electron.,* vol. 36, no. 2, pp. 1870–1882, Feb. 2021.

[7] H. Zhou, Z. Shen, Y. Wu, X. Chen, and Y. Zhang, "A stable dynamic electric vehicle wireless charging system based on triple decoupling receiving coils and a novel triple-diode rectifier," *IEEE Trans. Ind. Electron.,* vol. 71, no. 10, pp. 12011–12018, Oct. 2024.

[8] Y. Zhang, C. Liu, M. Zhou, and X. Mao, "A novel asymmetrical quadrupolar coil for interoperability of unipolar, bipolar, and quadrupolar coils in electric vehicle wireless charging systems," *IEEE Trans. Ind. Electron.,* vol. 71, no. 4, pp. 4300–4303, Apr. 2024.

[9] B. Song, S. Cui, Y. Li, and C. Zhu, "A fast and general method to calculate mutual inductance for EV dynamic wireless charging system," *IEEE Trans. Power Electron.,* vol. 36, no. 3, pp. 2696–2709, Mar. 2021.

[10] P. Zhang, M. Saeedifard, O. C. Onar, Q. Yang, and C. Cai, "A field enhancement integration design featuring misalignment tolerance for wireless EV charging using LCL topology," *IEEE Trans. Power Electron.,* vol. 36, no. 4, pp. 3852–3867, Apr. 2021.

[11] V. Z. Barsari, D. J. Thrimawithana, and G. A. Covic, "An inductive coupler array for in-motion wireless charging of electric vehicles," *IEEE Trans. Power Electron.,* vol. 36, no. 9, pp. 9854–9863, Sep. 2021.

[12] R. Xie, Y. Wu, H. Tang, and Y. Zhuang, "A strongly coupled vehicle-to-vehicle wireless charging system for emergency charging purposes with constant-current and constant-voltage charging capabilities," *IEEE Trans. Power Electron.,* vol. 39, no. 4, pp. 3985–3989, Apr. 2024.

[13] S. Niu, Q. Zhao, H. Chen, S. Niu, and L. Jian, "Noncooperative metal object detection using pole-to-pole EM distribution characteristics for wireless EV charger employing DD coils," *IEEE Trans. Ind. Electron.,* vol. 71, no. 6, pp. 6335–6344, Jun. 2024.

[14] Z. Sun, Y. Wang, and M. Li, "Analysis and design of 6.78M WPT architecture for configurable power applications based on DCX energy synthesis and functional execution," *IEEE Trans. Power Electron.,* vol. 39, no. 1, pp. 106–111, Jan. 2024.

[15] Y. Cheng, Y. Guan, T. Yao, Y. Wang, W. Wang, and D. Xu, "Topology construction strategy of load-independent single-switch resonant inverter," *IEEE Trans. Ind. Electron.,* vol. 71, no. 9, pp. 10580–10590, Sep. 2024.

[16] E. Chung and J. I. Ha, "Impedance matching network design for 6.78-MHz wireless power transfer system with constant power characteristics against misalignment," *IEEE Trans. Power Electron.,* vol. 39, no. 1, pp. 1788–1801, Jan. 2024.

[17] Z. Li, Q. Chen, S. Zhang, X. Ren, and Z. Zhang, "A novel domestic SE-IH with high induction efficiency and compatibility of nonferromagnetic vessels," *IEEE Trans. Ind. Electron.,* vol. 68, no. 9, pp. 8006–8016, Sep. 2021.

[18] Y. D. Lee, K. W. Kim, and G. W. Moon, "A self-compensated planar coil with integrated single-switch regulator for wireless power transfer (WPT) systems," *IEEE Trans. Ind. Electron.,* vol. 36, no. 10, pp. 10954–10958, Oct. 2021.

[19] J. Wang and Z. Huang, "A single-switch WPT circuit with inherent CCO-CVO for battery charging," *IEEE Trans. Transp. Electrif.,* vol. 10, no. 1, pp. 1957–1968, Mar. 2024.

[20] H. Yuan, C. Wang, and D. Xia, "Research on input-parallel single-switch WPT system with load-independent constant voltage output," *IEEE Trans. Transp. Electrif.,* vol. 9, no. 1, pp. 1888–1896, Mar. 2023.

[21] Q. Zhang, C. Wang, H. Yuan, and S. Zhang, "Research on input-parallel single-switch wireless power transfer system with constant-current and constant-voltage output," *IEEE Trans. Power Electron.,* vol. 37, no. 4, pp. 4817–4830, Apr. 2022.

[22] H. Li, M. Liu, L. Kong, and Y. Wang, "An independent dual-coil driving topology for wireless power transfer," *IEEE Trans. Power Electron.,* vol. 38, no. 2, pp. 1378–1383, Feb. 2023.

[23] H. Li, Z. Liu, B. Pan, and Y. Wang, "A wireless power transfer system with high misalignment tolerance and low component count," *IEEE Trans. Power Electron.,* vol. 39, no. 3, pp. 3774–3786, Mar. 2024.

[24] Z. Guo, C. Wang, S. Lin, L. Yang, and X. Lu, "Multiparallel and flexible expansion of single-switch WPT inverter by magnetic integration," *IEEE Trans. Power Electron.,* vol. 38, no. 3, pp. 4167–4180, Mar. 2023.

[25] J. T. Boys, G. A. Covic, and A. W. Green, "Stability and control of inductively coupled power transfer systems," *IEE Proc. Electr. Power Appl.,* vol. 147, no. 1, pp. 37–43, 2000.

[26] Z. Dai and J. Wang, "A dual-frequency WPT based on multilayer self-decoupled compact coil and dual CLCL hybrid compensation topology," *IEEE Trans. Power Electron.,* vol. 37, no. 11, pp. 13955–13965, Nov. 2022.

[27] S. Aldhaher, D. C. Yates, and P. D. Mitcheson, "Load-independent Class E/EF inverters and rectifiers for MHz-switching applications," *IEEE Trans. Power Electron.,* vol. 33, no. 10, pp. 8270-8287, Oct. 2018.

Jingyu Wang was born in Tai An, China, in 1996. He received a B.S. degree in electrical engineering and automation from Hefei University of Technology, Hefei, China, in 2019 and an M.S. degree in electrical engineering from Qingdao University, Qingdao, China, in 2022. He is currently working toward a Ph.D. degree in Shien-Ming Wu School of Intelligent Engineering, South China University of Technology, Guangzhou, China.

His current research interests mainly include wireless power transfer.

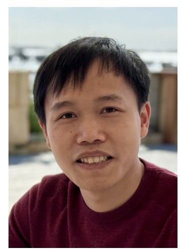

Zhicong Huang (Senior Member, IEEE) received the B.Eng. degree in electrical engineering and automation and the M.Eng. degree in mechanical and electronic engineering from the Huazhong University of Science and Technology, Wuhan, China, in 2010 and 2013, respectively, and the Ph.D. degree in power electronics from The Hong Kong Polytechnic University, Hong Kong, in 2018.

In 2019, he was a Postdoctoral Fellow under the UM Macao Talent Program with the State Key Laboratory of Analog and Mixed-Signal VLSI, Macau, China. Since 2020, he has been an Associate Professor with the Shien-Ming Wu School of Intelligent Engineering, South China University of Technology, Guangzhou, China. His research interests include wireless power transfer, artificial intelligence in power electronics, and wave energy converters.

Dr. Huang received the Outstanding Reviewer Award for IEEE Transactions on Power Electronics in 2021, the Star Reviewer Award for IEEE Journal on Emerging and Selected Topics in Power Electronics in 2023, and the Best Reviewer for IEEE Journal on Emerging and Selected Topics in Circuits and Systems in 2023. He servers as an Associate Editor for IEEE Transactions on Consumer Electronics.

Xiaolu Lucia Li (Member, IEEE) received the B.Eng. and M.Phil. degrees in electrical engineering from Harbin Institute of Technology, China, in 2014 and 2016, respectively, and the Ph.D. degree in power electronics from Hong Kong Polytechnic University, Hong Kong, in 2019. She is currently an Associate Professor of Integrated Circuits at Sun Yat-sen University, China. Prior to joining Sun Yat-sen University in November 2024, she was a Consultant with the Smart City Division, Hong Kong Productivity Council, and was a Postdoctoral Fellow with the Department of Electrical Engineering, City University of Hong Kong. Her research interests include multiport converters and wireless power transfer.